Published in final edited form as:

Angew Chem Int Ed Engl. 2021 June 01; 60(23): 12802–12806. doi:10.1002/anie.202102603.

A Terminal Imido Complex of an Iron–Sulfur Cluster

Arun Sridharan, **Alexandra C. Brown**, **Daniel L. M. Suess [Prof. Dr.]**

Department of Chemistry, Massachusetts Institute of Technology, 77 Massachusetts Ave, Cambridge MA 02139 (USA)

Abstract

We report the synthesis and characterization of the first terminal imido complex of an Fe–S cluster, $(IMes)_3Fe_4S_4$=NDipp (**2**; IMes = 1,3-dimesitylimidazol-2-ylidene, Dipp = 2,6-diisopropylphenyl), which is generated by oxidative group transfer from $DippN_3$ to the all-ferrous cluster $(IMes)_3Fe_4S_4(PPh_3)$. This two-electron process is achieved by formal one-electron oxidation of the imido-bound Fe site and one-electron oxidation of two IMes-bound Fe sites. Structural, spectroscopic, and computational studies establish that the Fe–imido site is best described as a high-spin Fe^{3+} center, which is manifested in its long Fe–N(imido) distance of 1.763(2) Å. Cluster **2** abstracts hydrogen atoms from 1,4-cyclohexadiene to yield the corresponding anilido complex, demonstrating competency for C–H activation.

Graphical Abstract

suess@mit.edu.

Supporting information for this article is given via a link at the end of the document.

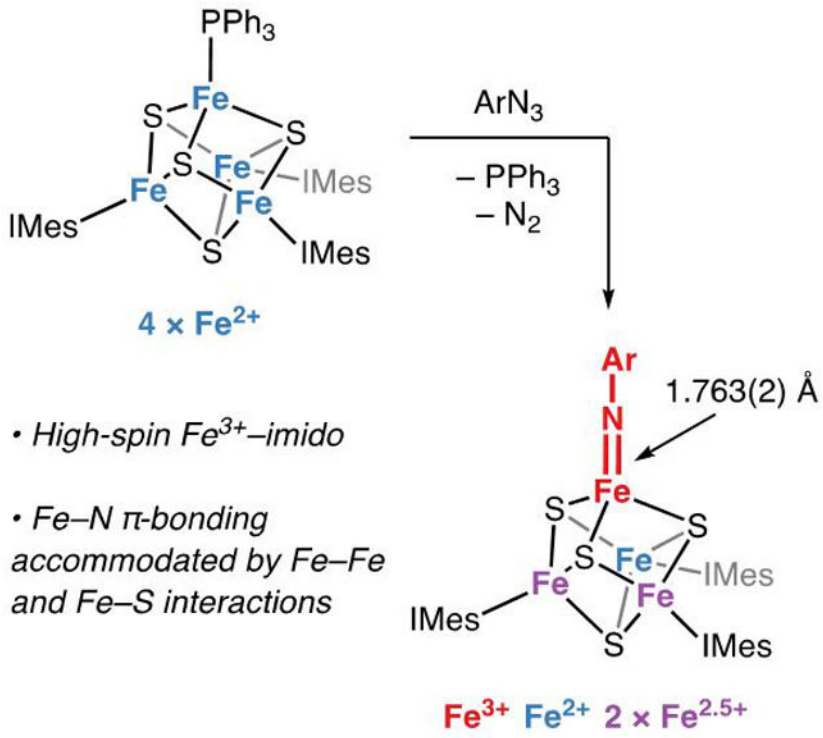

The first terminal imido complex of an iron–sulfur cluster has been synthesized and fully characterized. Structural, spectroscopic, and computational analysis suggest an $[Fe_4S_4]^{2+}$–$[NAr]^{2-}$ formulation with a localized high-spin Fe^{3+} valence at the imido-bound site, and reactivity studies demonstrate competency for C–H activation.

Keywords

Bioinorganic chemistry; C–H activation; Cluster compounds; Multiple bonds

Studies of terminal imido complexes of the transition metals continue to push the frontiers of metal–ligand multiple bonding and present new opportunities in catalysis.[1–5] In particular, terminal Fe–imidos have attracted interest in these regards and as models for plausible intermediates in biological nitrogen fixation.[6–12] However, it is unclear in what ways the findings from mononuclear Fe–imido chemistry would translate to the chemistry of Fe–S clusters (such as the catalytic cofactors of nitrogenases). This is in part because mononuclear Fe–imido complexes are themselves electronically diverse and have been characterized across a wide range of oxidation and spin states.[10,13,14] Moreover, the ability of Fe–S clusters to support Fe–N multiple bonding is not well-established, and it is not known how the quintessential electronic features of Fe–S clusters—weak ligand fields and significant Fe–Fe exchange coupling—would impact the Fe–N bonding in an Fe–imido group. Characterization of a synthetic Fe–S–imido cluster could address these questions, and although progress has been made in preparing terminal Fe–imidos in weak ligand fields,[15–20] polynuclear terminal Fe–imidos remain rare,[15,21] and no terminal imido complex of an Fe–S cluster has been reported. As such, we have begun investigating the chemistry of

Fe–S–imido clusters, and we herein report the synthesis and characterization of a terminal imido complex of an $[Fe_4S_4]$ cluster.

A common route to metal–imido complexes entails two-electron oxidation with a nitrene group transfer reagent such as an organic azide. To extend this methodology to an Fe–S cluster, we used the $(IMes)_3Fe_4S_4$ platform (IMes = 1,3-dimesitylimidazol-2-ylidene), which features a cuboidal $[Fe_4S_4]$ cluster in which three Fe sites are supported by IMes ligands and the remaining Fe site is available for reaction chemistry.[22] Mild, one-electron reduction of the previously reported cluster $(IMes)_3Fe_4S_4Cl$ was achieved via Cl-atom abstraction using Cummins's reagent $Ti(N[^tBu]Ar)_3$ (Ar = 3,5-dimethylphenyl).[23] The resulting all-ferrous, $[Fe_4S_4]^0$ cluster was trapped using PPh_3 to produce $(IMes)_3Fe_4S_4(PPh_3)$ (**1**) in 77% yield (Scheme 1). Room-temperature addition of 1 equiv 2,6-diisopropylphenyl azide ($DippN_3$) to **1** in C_6D_6 resulted in an immediate color change from red-brown to green-brown. ^1H NMR analysis of the reaction mixture revealed production of 1 equiv PPh_3 as well as the terminal imido complex $(IMes)_3Fe_4S_4$=NDipp (**2**; Scheme 1), whose structure was confirmed by single-crystal X-ray diffraction (vide infra). Although **2** is sufficiently stable for most characterization techniques, it slowly degrades in solution to give a mixture of species including the anilido complex $(IMes)_3Fe_4S_4$–N(H)Dipp (**3**), which was independently synthesized and characterized (see SI); **3** can also be cleanly generated from **2** via H-atom abstraction from weak C–H bonds (vide infra).

Cluster **2** exhibits C_{3v} symmetry in solution with contact-shifted resonances between +16 and −4.5 ppm in its room-temperature ^1H NMR spectrum (Figure S2). The modest shifting of the ^1H resonances suggests that **2**, like nearly all other $[Fe_4S_4]^{2+}$ clusters,[24,25] features an $S = 0$ ground state with some thermal population of paramagnetic excited states. The diamagnetic ground state of **2** was confirmed by variable-temperature SQUID magnetometry measurements, which exhibit $\chi_M T$ values near 0 cm^3 K mol^{-1} between 2 and 80 K (Figure S12).

The solid-state structure of **2** (Figure 1)[26] reveals an Fe–N bond length of 1.763(2) Å, which is among the longest Fe–N distances reported for crystallographically characterized Fe–NR complexes (R = aryl, alkyl).[27] The average Fe–N distance in four-coordinate Fe–NR complexes is 1.66 Å (Figure S19); such short bond lengths reflect low- or intermediate-spin electronic configurations with unoccupied Fe–N π* orbitals and Fe–N triple bond character (see Table S10 for representative examples). Notable exceptions include a pair of high-spin Fe^{3+}–aryliminyl ($[NAr]^{\bullet-}$) complexes with Fe–N bond lengths of 1.766(4) and 1.768(2) Å, respectively, and an Fe^{3+}–alkyliminyl complex with an Fe–N bond length of 1.761(7) Å; all three feature Fe–N bond lengths nearly identical to that observed for **2**.[19,28,29] The long Fe–N distance in **2** therefore indicates a high-spin configuration at the unique Fe site, attenuated Fe–N multiple bonding, and perhaps contribution from an iminyl-type electronic configuration (vide infra). However, we note that the computed Fe–N bond lengths in the hypothetical, tetrahedral model complexes $[Cl_3Fe(NPh)]^{2-}$ (high-spin Fe^{3+}–imido) and $[Cl_3Fe(NPh)]^-$ (high-spin Fe^{3+}–iminyl) are identical (1.76 Å; see Table S8), and as such, the redox state of the [NAr] fragment in **2** cannot be unambiguously inferred from the Fe–N bond length.

Because of the propensity for terminal Fe–imido complexes to exhibit high Fe–N covalency, we anticipated that the Fe–S cluster core of **2** could be geometrically and/or electronically distinct from those of typical $[Fe_4S_4]$ clusters. Interestingly, however, the cluster's Fe–Fe and Fe–S distances fall within typical ranges for $[Fe_4S_4]^n$ clusters (n = 1+, 2+, 3+)[30] including other structurally characterized members of the $(IMes)_3Fe_4S_4$ family.[22,31] The $[Fe_4S_4]$ core of **2** exhibits a characteristic tetragonal compression from idealized T_d symmetry, with eight long Fe–S bonds (avg. 2.316(2) Å) defining two opposing $[Fe_2S_2]$ rhombs, and four short Fe–S bonds (avg. 2.241(1) Å) that connect the two rhombs (Figure 1B).[32] The average Fe–S bond length for the imido-bound Fe (2.310(1) Å) is ca. 0.04 Å longer than those of the IMes-bound sites (vide infra). The modestly elongated—rather than significantly shortened—Fe–S distances at the imido-bound Fe site suggest that it does not adopt a locally high-valent state (e.g., Fe^{4+}, as was observed for the structurally related cluster $[Fe_4(\mu_3\text{-}N^tBu)_4(N^tBu)Cl_3]$[15]) and is instead consistent with a local valence in the Fe^{2+}–Fe^{3+} range as is typically observed in Fe–S clusters. Taken together, the unusually long Fe–N bond length and unexceptional cluster core metrics of **2** support a high-spin, mid-valent (Fe^{2+} or Fe^{3+}) configuration for the imido-bound Fe.

To further investigate the electronic structure of **2**, we undertook a combined Mössbauer spectroscopic and computational study. The 90 K ^{57}Fe Mössbauer spectrum of **2** is relatively sharp (Figure 2) and several simulations fit the data satisfactorily (Figures 2 and S13 and Tables 1 and S1). Before further discussing the simulation, we note some observations based on the spectrum itself. The absence of a quadrupole doublet centered at or below ca. 0 mm s^{-1} precludes the presence of either a valence-localized Fe^{4+} ion or a low-spin Fe^{3+} imido site (see Table S10 for comparisons); this interpretation is consistent with the structural observations discussed above. In addition, the spectral centroid of the Mössbauer spectrum of **2** (0.43 mm s^{-1}) is significantly lower than that of $[Fe_4S_4]^+$–anilido cluster **3** (0.53 mm s^{-1}; Figure S14); this difference is similar to that observed for other $[Fe_4S_4]^{2+/+}$ clusters[33] and is indicative of substantial charge depletion of the Fe sites in **2** relative to those in **3**. On this basis, as well as the computational studies described below, we conclude that the contribution of an $[Fe_4S_4]^+$–iminyl configuration to the electronic structure of **2** is likely minor and that **2** is best described as an $[Fe_4S_4]^{2+}$ cluster with a closed-shell imido ($[NAr]^{2-}$) ligand.

Broken-symmetry density functional theory (BS DFT) calculations were carried out on a truncated model of **2** to aid in interpretation of its electronic structure and Mössbauer spectrum. Several BS determinants were evaluated, and in all cases the [NAr] fragment converged to a closed-shell, $[NAr]^{2-}$ configuration (see SI). The lowest-energy determinant is characterized by an electronic configuration in which the Fe spins are coaligned within each crystallographically observed $[Fe_2S_2]$ rhomb, with the two rhombs antiferromagnetically coupled to one another; this picture corresponds to the usual coupling pattern for an $S = 0$ $[Fe_4S_4]^{2+}$ cluster.[24,25] The calculated Mössbauer parameters (Table 1) include isomer shifts (δ) of 0.40 and 0.50 mm s^{-1} for the imido-bound Fe and the spin-aligned IMes-bound Fe, respectively, with the remaining two IMes-bound Fe sites in the opposing $[Fe_2S_2]$ rhomb taking on isomer shifts similar to that of the imido site (0.42 and 0.40 mm s^{-1}) but with significantly smaller quadrupole splittings ($|\Delta E_Q|$). This approximate

1:2:1 pattern of quadrupole doublets is well-accommodated by the experimental Mössbauer spectrum (Figure 2) and is reflected in our preferred simulation, though we again caution that the data can be fit by several parameter sets (see Table S1).

To facilitate interpretation of the bonding in **2**, the BS DFT-derived canonical orbitals were localized,[34] and Löwdin population analyses were used to derive formal oxidation states (FOSs) of each site (Table 1 and Figure 3; see SI for details). The picture that emerges is a perturbation of the canonical Heisenberg double-exchange model for $[Fe_4S_4]^{2+}$ clusters.[24,25] Each Fe site has five singly occupied 3d orbitals in the α (or β) manifold, with an additional electron delocalized between pairs of Fe centers in the β (or α) manifold (Figure 3A). As expected, the two double-exchange-coupled, IMes-ligated Fe sites evenly share their itinerant electron (Figure 3B, left), leading to FOSs of 2.52+ and 2.55+, respectively (consistent with their similar Mössbauer isomer shifts in Table 1). In contrast, the double-exchange interaction between the imido-bound Fe site and its spin-aligned coupling partner is significantly polarized (Figure 3B, right), with FOSs approaching complete valence trapping (2.91+ and 2.16+, respectively). This electronic buffering is reminiscent of that observed for alkylated $[Fe_4S_4]^{2+}$ clusters in which the strongly donating alkyl group induces partial localization of Fe^{3+} character at the alkyl-bound Fe with concomitant localization of Fe^{2+} character at its spin-aligned partner.[35,36]

Although we conclude that the imido-bound Fe site is best described as Fe^{3+}, it is noteworthy that its Mössbauer isomer shift is essentially identical to those observed and calculated for the formally more reduced $Fe^{2.5+}$–IMes sites (Table 1). The relatively high isomer shift for the Fe–imido site can be rationalized by considering the impact of local symmetry on Fe–N and Fe–S covalency: the singly occupied orbitals with Fe–N **π*** character are also antibonding with respect to the Fe–S bonds, and therefore destabilization of these orbitals due to Fe–N **π** bonding is compensated by lengthening of the Fe–S bonds, as reflected in the bond metrics (Figure 1B). In this manner, the Fe–N covalency, which lowers the Mössbauer isomer shift, is in part offset by a symmetry-enforced decrease in Fe–S covalency. Overall, these findings demonstrate a dynamic interplay between Fe–N, Fe–S, and Fe–Fe bonding in Fe–S clusters featuring Fe–N multiple bonding.

Preliminary reactivity studies of **2** demonstrate its proclivity for H-atom abstraction. Exposure of a solution of **2** in Et_2O to excess 1,4-cyclohexadiene (C–H bond dissociation free energy (BDFE) in Et_2O of 72.2 kcal mol^{-1})[37] results in clean conversion to anilido complex **3** over 1 h with concomitant formation of 0.5 equiv benzene (Scheme 2 and Figure S6). Cluster **2** does not abstract H-atoms from toluene (C–H BDFE in benzene of 86.5 kcal mol^{-1})[37] at room temperature or at 50 °C, with no 1,2-diphenylethane detected by ^1H NMR spectroscopy under these conditions (Figures S7 and S8). Taken together, these observations suggest that **2**, like other high-spin[19,28,29,38] as well as some transiently observed or inferred intermediate-[16,39–41] and low-spin[42,43] Fe–NR complexes, is competent for activation of weak C–H bonds, and that the N–H BDFE of **3** is between ca. 72 and 87 kcal mol^{-1}.

In conclusion, an $[Fe_4S_4]$ cluster with a terminal imido ligand was prepared by oxidative group transfer between an organic azide and an all-ferrous $[Fe_4S_4]$ cluster; the cluster's

reducing equivalents are formally derived from the imido-bound Fe site as well as a pair of IMes-ligated Fe sites. The local high-spin state of the Fe^{3+}–imido unit results in attenuated Fe–N multiple bonding and imbues H-atom abstraction reactivity. Overall, this study establishes the ability of Fe–S clusters to support Fe–ligand multiple bonding, demonstrates how the plasticity of Fe–S and Fe–Fe interactions accommodates covalent Fe–N bonding, and links the rich chemistry of Fe–imidos with Fe–S cluster model chemistry. Further studies on the reactivity of **2** and related complexes are underway.

Supplementary Material

Refer to Web version on PubMed Central for supplementary material.

Acknowledgements

We thank Dr. Peter Müller for assistance with XRD experiments, Dr. Patrick Smith for assistance with collecting SQUID magnetometry data, and Dr. Niklas Thompson for helpful discussions. Research reported in this publication was supported by MIT Research Support Committee Funds and the National Institute of General Medical Sciences of the National Institutes of Health under award number R01GM136882.

References

[1]. Nugent WA, Mayer JM, Metal-Ligand Multiple Bonds: The Chemistry of Transition Metal Complexes Containing Oxo, Nitrido, Imido, Alkylidene, Or Alkylidyne Ligands, Wiley, New York, 1988.

[2]. Kawakita K, Parker BF, Kakiuchi Y, Tsurugi H, Mashima K, Arnold J, Tonks IA, Coord. Chem. Rev 2020, 407, 213118. [PubMed: 32863399]

[3]. Eikey RA, Abu-Omar MM, Coord. Chem. Rev 2003, 243, 83–124.

[4]. Ray K, Heims F, Pfaff FF, Eur. J. Inorg. Chem 2013, 3784–3807.

[5]. Park Y, Kim Y, Chang S, Chem. Rev 2017, 117, 9247–9301. [PubMed: 28051855]

[6]. Mehn MP, Peters JC, J. Inorg. Biochem 2006, 100, 634–643. [PubMed: 16529818]

[7]. Wang P, Deng L, Chin. J. Chem 2018, 36, 1222–1240.

[8]. Plietker B, Röske A, Catal. Sci. Technol 2019, 9, 4188–4197.

[9]. Jia Z-J, Gao S, Arnold FH, J. Am. Chem. Soc 2020, 142, 10279–10283. [PubMed: 32450692]

[10]. Saouma CT, Peters JC, Coord. Chem. Rev 2011, 255, 920–937. [PubMed: 21625302]

[11]. Buratto WR, Murray LJ, in Reference Module in Chemistry, Molecular Sciences, and Engineering, Elsevier, 2020, DOI: 10.1016/B978-0-12-409547-2.14822-X.

[12]. Chalkley MJ, Drover MW, Peters JC, Chem. Rev 2020, 120, 5582–5636. [PubMed: 32352271]

[13]. Berry JF, Comments Inorg. Chem 2009, 30, 28–66.

[14]. Suarez AIO, Lyaskovskyy V, Reek JNH, van der Vlugt JI, de Bruin B, Angew. Chem. Int. Ed 2013, 52, 12510–12529.

[15]. Verma AK, Nazif TN, Achim C, Lee SC, J. Am. Chem. Soc 2000, 122, 11013–11014.

[16]. Klinker EJ, Jackson TA, Jensen MP, Stubna A, Juhász G, Bominaar EL, Münck E, Que L, Angew. Chem. Int. Ed 2006, 45, 7394–7397.

[17]. Cowley RE, DeYonker NJ, Eckert NA, Cundari TR, DeBeer S, Bill E, Ottenwaelder X, Flaschenriem C, Holland PL, Inorg. Chem 2010, 49, 6172–6187. [PubMed: 20524625]

[18]. Bowman AC, Milsmann C, Bill E, Turner ZR, Lobkovsky E, Debeer S, Wieghardt K, Chirik PJ, J. Am. Chem. Soc 2011, 133, 17353–17369. [PubMed: 21985461]

[19]. Wilding MJT, Iovan DA, Wrobel AT, Lukens JT, MacMillan SN, Lancaster KM, Betley TA, J. Am. Chem. Soc 2017, 139, 14757–14766. [PubMed: 28937756]

[20]. Hong S, Sutherlin KD, Vardhaman AK, Yan JJ, Park S, Lee Y-M, Jang S, Lu X, Ohta T, Ogura T, Solomon EI, Nam W, J. Am. Chem. Soc 2017, 139, 8800–8803. [PubMed: 28628312]

[21]. Kuppuswamy S, Powers TM, Johnson BM, Bezpalko MW, Brozek CK, Foxman BM, Berben LA, Thomas CM, Inorg. Chem 2013, 52, 4802–4811. [PubMed: 23259457]

[22]. Brown AC, Suess DLM, Inorg. Chem 2019, 58, 5273–5280. [PubMed: 30901206]

[23]. Peters JC, Johnson AR, Odom AL, Wanandi PW, Davis WM, Cummins CC, J. Am. Chem. Soc 1996, 118, 10175–10188.

[24]. Beinert H, Holm RH, Münck E, Science 1997, 277, 653–659. [PubMed: 9235882]

[25]. Noodleman L, Peng CY, Case DA, Mouesca J-M, Coord. Chem. Rev 1995, 144, 199–244.

[26]. CCDC 2062855 (2) and 2062854 (3) contain the supplementary crystallographic data for this paper. These data can be obtained free of charge from The Cambridge Crystallographic Data Centre via www.ccdc.cam.ac.uk/structures.

[27]. Groom CR, Bruno IJ, Lightfoot MP, Ward SC, Acta Crystallogr. Sect. B Struct. Sci. Cryst. Eng. Mater 2016, 72, 171–179.

[28]. King ER, Hennessy ET, Betley TA, J. Am. Chem. Soc 2011, 133, 4917–4923. [PubMed: 21405138]

[29]. Iovan DA, Betley TA, J. Am. Chem. Soc 2016, 138, 1983–1993. [PubMed: 26788747]

[30]. Tan LL, Holm RH, Lee SC, Polyhedron 2013, 58, 206–217. [PubMed: 24072952]

[31]. Brown AC, Suess DLM, J. Am. Chem. Soc 2020, 142, 14240–14248. [PubMed: 32696642]

[32]. Uncertainties for average distances are given as the root sum of the squares of the individual estimated standard deviations.

[33]. Venkateswara Rao P, Holm RH, Chem. Rev 2004, 104, 527–559. [PubMed: 14871134]

[34]. Knizia G, Chem J. Theory Comput. 2013, 9, 4834–4843.

[35]. Ye M, Thompson NB, Brown AC, Suess DLM, J. Am. Chem. Soc 2019, 141, 13330–13335. [PubMed: 31373801]

[36]. McSkimming A, Sridharan A, Thompson NB, Müller P, Suess DLM, J. Am. Chem. Soc 2020, 142, 14314–14323. [PubMed: 32692919]

[37]. Solution phase BDFEs were computed as described in:Warren JJ, Tronic TA, Mayer JM, Chem. Rev 2010, 110, 6961–7001. [PubMed: 20925411] Values for the solubility of H2 in Et2O and benzene taken from:Solubility Data Series Volume 5/6: Hydrogen and Deuterium (Ed.: Young CL), Pergamon, Oxford, 1981.

[38]. Wilding MJT, Iovan DA, Betley TA, J. Am. Chem. Soc 2017, 139, 12043–12049. [PubMed: 28777558]

[39]. Cowley RE, Eckert NA, Vaddadi S, Figg TM, Cundari TR, Holland PL, J. Am. Chem. Soc 2011, 133, 9796–9811. [PubMed: 21563763]

[40]. Lucas RL, Powell DR, Borovik AS, J. Am. Chem. Soc 2005, 127, 11596–11597. [PubMed: 16104724]

[41]. Gouré E, Avenier F, Dubourdeaux P, Sénèque O, Albrieux F, Lebrun C, Clémancey M, Maldivi P, Latour J-MM, Angew. Chem. Int. Ed 2014, 53, 1580–1584.

[42]. Mankad NP, Müller P, Peters JC, J. Am. Chem. Soc 2010, 132, 4083–4085. [PubMed: 20199026]

[43]. Spasyuk DM, Carpenter SH, Kefalidis CE, Piers WE, Neidig ML, Maron L, Chem. Sci 2016, 7, 5939–5944. [PubMed: 30034736]

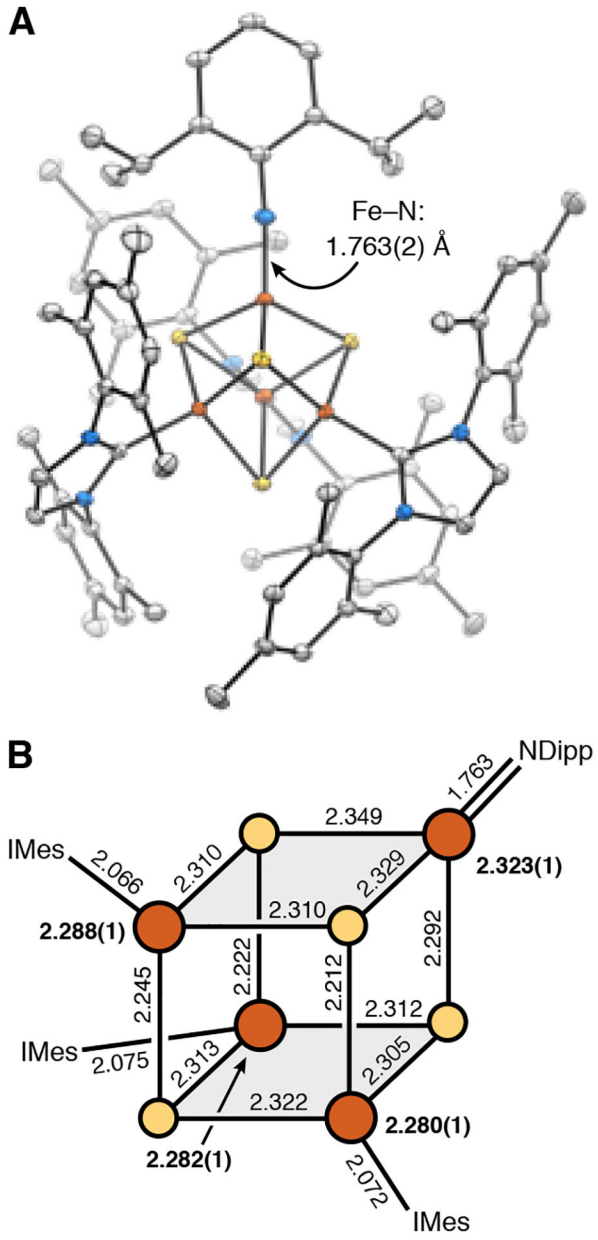

Figure 1.

(**A**) Thermal ellipsoid plot (50%) of **2**. Orange, yellow, gray, and blue represent Fe, S, C, and N respectively. H atoms and solvent molecules omitted for clarity. (**B**) Schematic of **2** depicting the bond distances in Å. Rhombs containing parallel spin-aligned Fe atoms are highlighted in gray. Average Fe−S bond lengths for each site are shown in bold.[32] Standard uncertainties for individual distances have been omitted for clarity.

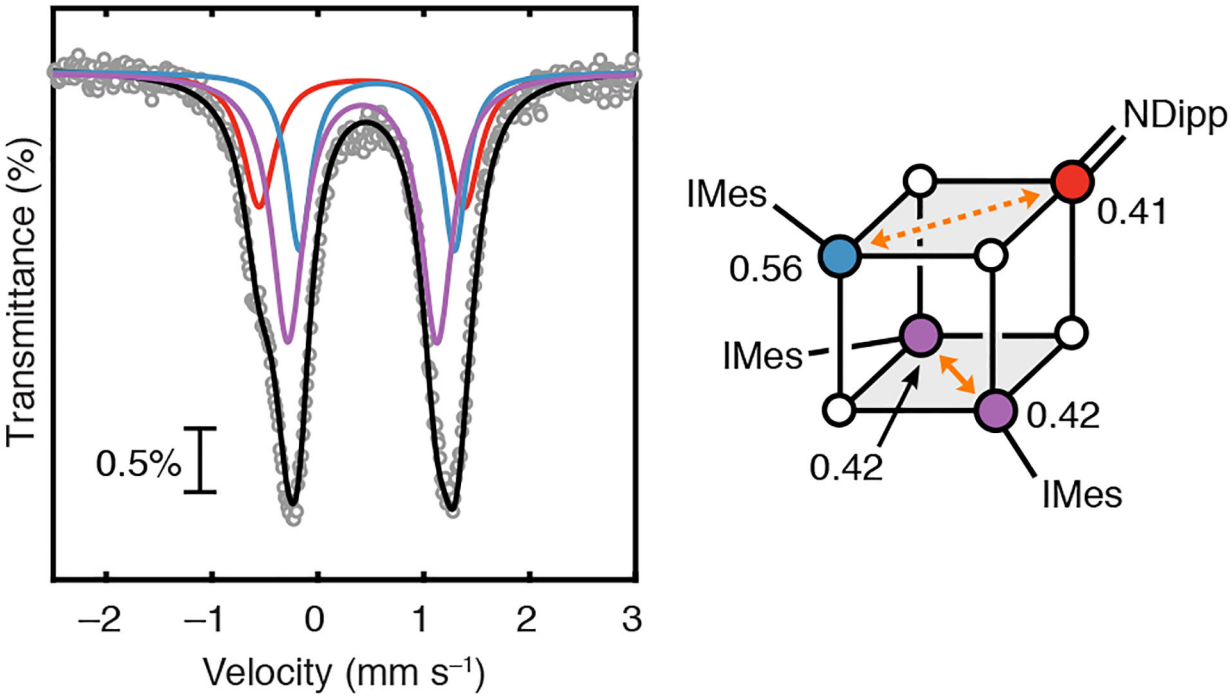

Figure 2.

Zero-field ^{57}Fe Mössbauer spectrum (90 K) of **2** with experimental data (circles), total simulation (black), and simulation components (colors as shown to the right). Isomer shifts for each site shown in mm s^{-1}. Solid and dotted orange lines indicate equally distributed and polarized double-exchange interactions, respectively.

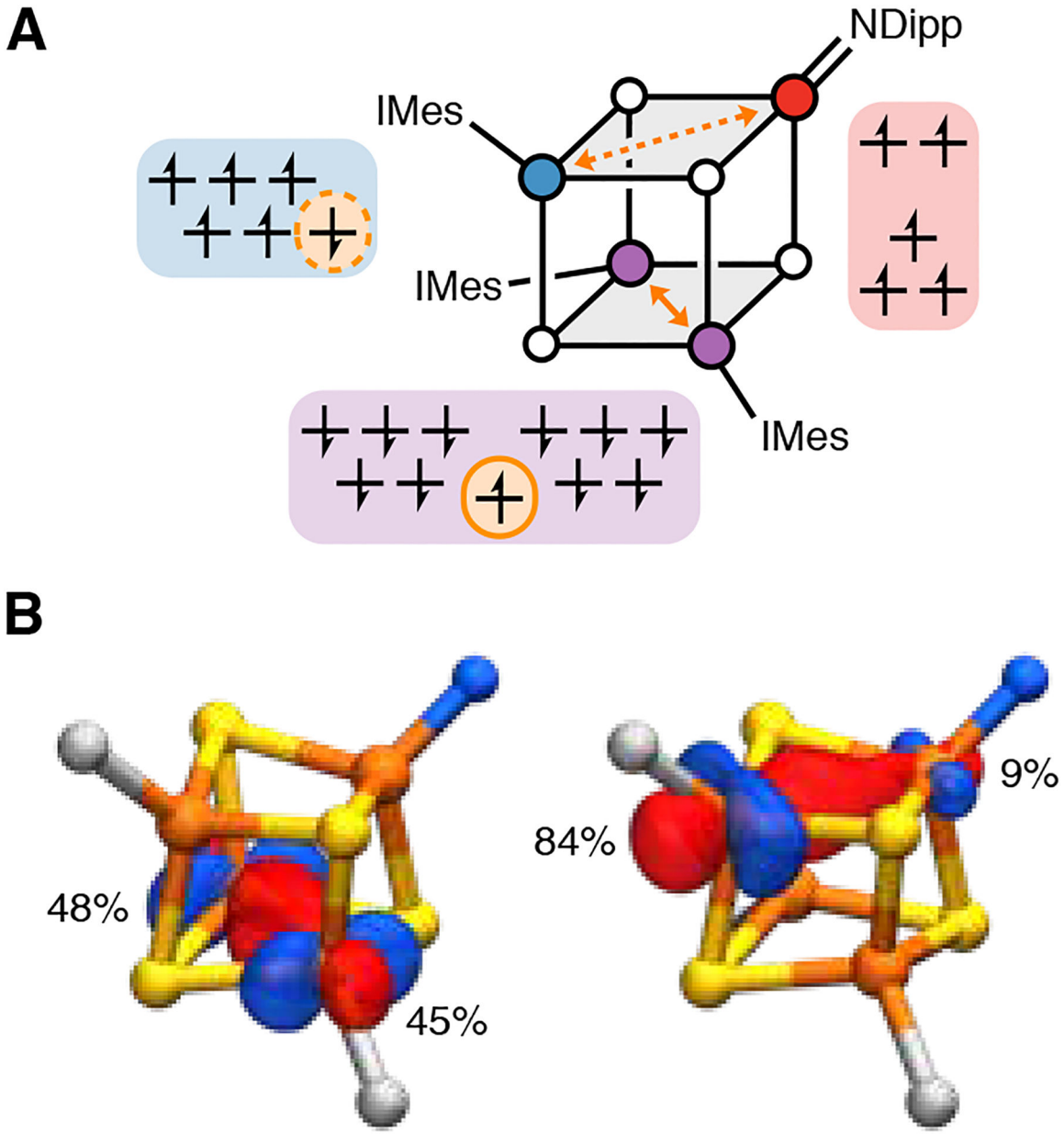

Figure 3.

(**A**) Qualitative 3d orbital diagrams of the Fe centers in **2** derived from BS DFT calculations. Coloring scheme is as in Figure 2. Orange circles highlight the delocalized electron within mixed-valent pairs. (**B**) Isosurface plots (0.05 au) of the local Fe contributions (obtained from a Löwdin population analysis) to the double-exchange interactions in the α (*left*) and β (*right*) manifolds. NHC ligands and N–Ar substituent represented by C and N atoms, respectively. Coloring scheme is as in Figure 1.

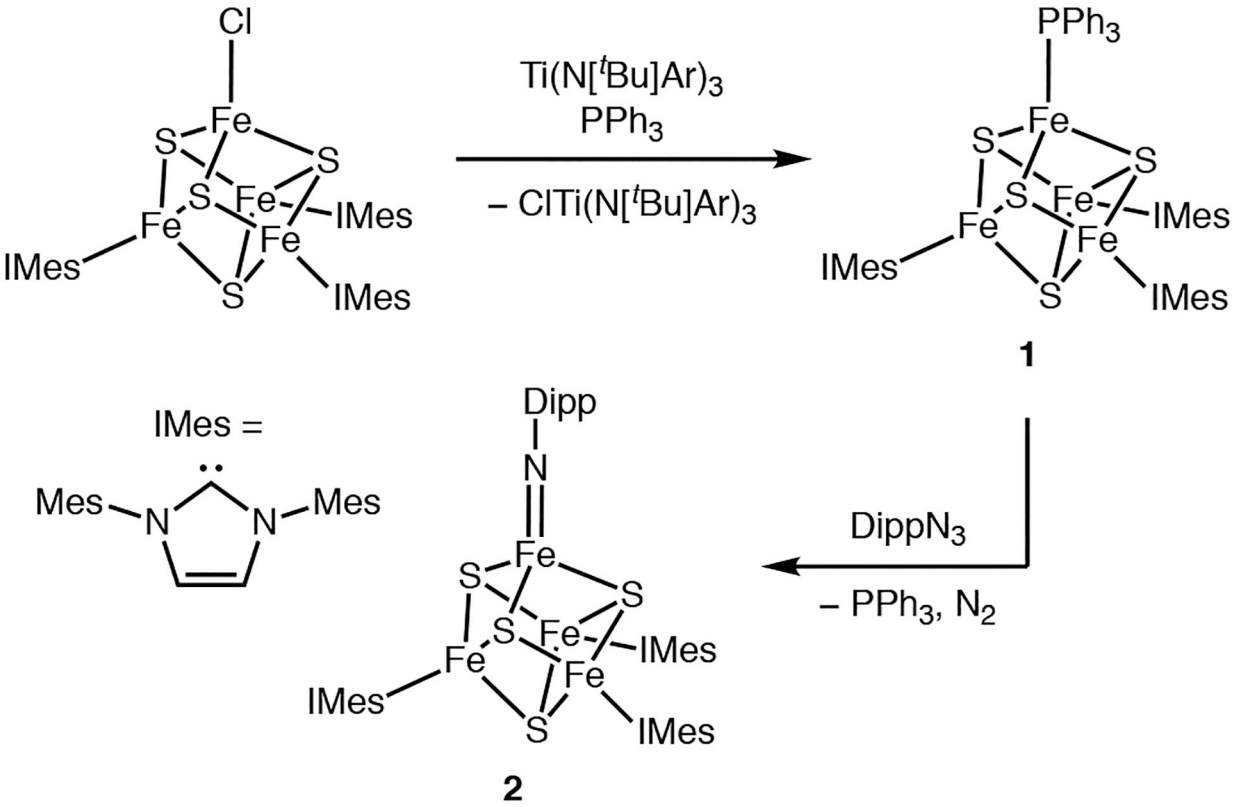

Scheme 1.

Synthesis of $(IMes)_3Fe_4S_4$=NDipp (**2**). Abbreviations: Mes = 2,4,6-trimethylphenyl; Ar = 3,5-dimethylphenyl; Dipp = 2,6-diisopropylphenyl.

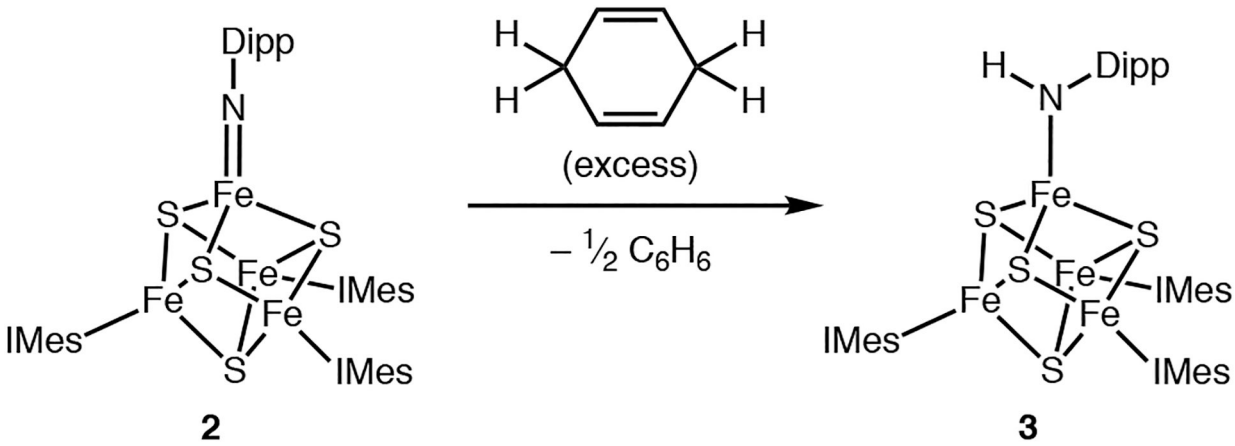

Scheme 2.

Reaction of **2** with 1,4-cyclohexadiene yields the anilido complex **3**.

Table 1.

Experimental (90 K) and calculated Mössbauer parameters for **2**[a]

Site	δ[b] (mm s^{-1})	$\lvert\Delta E_Q\rvert$[c] (mm s^{-1})	Area (%)	FOS[d]
Fe^{3+}=NDipp	0.41 (0.40)	1.94 (2.32)	25	2.91+
Fe^{2+}–IMes	0.56 (0.50)	1.47 (2.32)	25	2.16+
2 × $Fe^{2.5+}$–IMes	0.42 (0.42, 0.40)	1.41 (1.11, 1.04)	50	2.52+, 2.55+

[a]Calculated parameters in parentheses.

[b]Isomer shift.

[c]Quadrupole splitting.

[d]Formal oxidation states (FOSs) determined from Löwdin population analysis of the localized MOs for the lowest-energy broken-symmetry determinant (see SI).